Two-dimensional Superstructures of Silica Cages

*Tangi Aubert†, Kai Ma†, Kwan W. Tan, and Ulrich Wiesner**

Dr. T. Aubert, Dr. K. Ma, Prof. K. W. Tan, Prof. U. Wiesner

Department of Materials Science Engineering, Cornell University, Ithaca, NY 14853, USA.

E-mail: ubw1@cornell.edu

Dr. T. Aubert

Department of Chemistry, Ghent University, Ghent, 9000, Belgium.

Prof. K. W. Tan

Present Address: School of Materials Science and Engineering, Nanyang Technological University, Singapore 639798, Singapore.

Keywords: 2D materials, ultrathin membranes, ordered porous materials, Frank-Kasper, dual structures

Abstract

Despite extensive studies on mesoporous silica since the early 1990's, the synthesis of two-dimensional (2D) silica nanostructures remains challenging. Here, we synthesized mesoporous silica at an interface between two immiscible solvents under conditions leading to the formation of 2D superstructures of silica cages, the thinnest mesoporous silica films synthesized to date. Orientational correlations between cage units increase with increasing layer number controlled via pH, while swelling with oil and mixed surfactants increase micelle size dispersity, leading to complex clathrate type structures in multilayer superstructures. Results suggest that three-

dimensional (3D) crystallographic registry within cage-like superstructures emerges as a result of the concerted 3D co-assembly of organic and inorganic components. Mesoporous 2D superstructures can be fabricated over macroscopic film dimensions and stacked on top of each other. We envision realization of previously inaccessible mesoporous silica heterostructures with separation or catalytic properties unachievable via conventional bulk syntheses.

Main text

Since the early reports on directed silica self-assembly[1], these materials and their derivatives in the bulk[2, 3], as films[4], and as nanoparticles[5, 6] have been the subject of extensive research efforts. Benign synthesis conditions, often in aqueous solutions at room temperature, concomitant low toxicity and favorable biocompatibility[7], continuous structure discovery[8-10], as well as their application potential across different areas, *e.g.* in catalysis[11], energy[12], and nanomedicine[6, 13], maintain high academic and industrial interest levels. Facile pore accessibility makes cage-like mesoporous silica particularly interesting[3, 8, 14]. Recently, we isolated individual silica cages, grown around single organic molecule-swollen micelles.[10] However, fundamental understanding of how order emerges from a single cage to a 3D superstructure remains limited. In an attempt to close this knowledge gap and help rationalize observed structure formation, we assembled mesoporous silica at an interface between two immiscible liquids. Careful variation of synthesis conditions allowed the formation of a number of different 2D cage-like silica superstructures with controlled number of layers.

Base-catalyzed hydrolysis of alkoxysilane precursors in water produces primary silica clusters of about 2 nm diameter[10, 15] that can further condense to form ultrasmall (< 10 nm) silica nanoparticles[16]. In the presence of cationic surfactants such as cetyltrimethylammonium bromide (CTAB), negatively charged clusters self-assemble into micelle-templated mesoporous silica[1], with sizes controllable down to single pore nanoparticles[17]. The addition of a pore expander increases micelle size, size dispersity, and deformability[9, 18], enabling cage-

like mesoporous structures. Numerous studies have identified bulk mesoporous materials formed from such cages as basic building blocks[3, 8, 19], including 5^{12}, $5^{12}6^2$, or $5^{12}6^3$ cages, where 5^x6^y refers to a cage made of *x* pentagonal and *y* hexagonal faces. In contrast, details of the self-assembly processes involved in their formation, in particular the transition from a single cage to a 3D superstructure, often remains obscure. In this work, the controlled growth of 2D cage-based mesoporous silica enabled the direct real-space observation of structure evolution and the emergence of 3D order in those superstructures, one layer at a time. To the best of our knowledge, no such single-layer mesoporous silica films have ever been reported. These superstructures constitute a hitherto unknown type of material bridging the field of mesoporous materials with that of 2D materials. For example, borrowing ideas from the field of 2D electronic materials[20], results open scalable synthetic approaches to mesoporous silica heterostacks with property profiles inaccessible to date.

Results and Discussion

In order to create large liquid-liquid interfacial area for the confined growth of 2D mesoporous superstructures, a relatively large amount of an oil phase, namely cyclohexane, was dispersed in an equivalent volume of water under vigorous stirring, forming large droplets stabilized by CTAB. Tetramethyl orthosilicate (TMOS) was combined with (3-aminopropyl) trimethoxy silane (APTMS) as silica sources. Under basic conditions, neutral aminopropyl groups of APTMS intercalate the surfactant layer due to their hydrophobicity[21], serving as anchor points for primary silica clusters at the oil-surfactant-water interface[15]. This nucleates silica layer growth at the surface of the oil droplets as verified by fluorescence microscopy (**Figure 1a-b**). After removal of surfactant and oil, the ultrathin silica layers enabled unambiguous real-space structure analysis via comparison of transmission electron microscopy (TEM) images with structure models, *i.e.* without having to rely on reciprocal space analysis from diffraction patterns. This revealed nanosheets with hexagonally packed pores (Figure 1b,

d) and uniform thickness of only 6-7 nm (Figure S1, Supporting Information). Closer inspection revealed internal pore structures (Figure 1d) very similar to separately synthesized silica cages (Figure 1c), including patterns with 2-, 3- and 5-fold symmetry (Figure S2, Supporting Information). Lateral views provided by folds (Figure 1e and Figure S3, Supporting Information) showed vertical struts and windows rather than solid walls, supporting the assumption that these 2D superstructures are made of a single-layer of cage-like building blocks. The varying strut patterns suggest that a number of different cage orientations and/or cage structures may co-exist in these single-layer 2D superstructures. In this regard, these single-layer superstructures may resemble 2D plastic crystals[22]. Long-range 2D hexagonal order is highlighted by fast Fourier transformation (FFT) of TEM images (Figure S4, Supporting Information). Detailed TEM analysis (Figure S4c, Supporting Information) shows that the building blocks of these single-layer superstructures exhibit very similar dimensions (pore, vertex and edge diameters) as individually synthesized cages[10], suggesting similarities in their formation mechanism. We speculate that negatively charged silica clusters adsorb at the water/oil interface attracted by positively charged CTAB surfactant head groups and further stabilized by the hydrophobic aminopropyl groups which intercalate with the CTAB layer[21]. Similar adsorption processes have recently been evidenced in EM images of CTAB micelles decorated with individual silica clusters,[18] an effect which is promoted by the deformability of the surfactant-water interface, which is enhanced by micelle swelling with hydrophobic molecules. In turn, the surfactant molecules wrap around these clusters, increasing the degree of interaction between the organic and inorganic components. In the current case, this creates negatively charged patches on the liquid substrate, which in turn attract CTAB micelles from the water phase that assemble as a single monolayer on the liquid substrate (Figure S5, Supporting Information). Further silica condensation around these micelles completes cage-like silica superstructure formation.

Increasing the amount of oil in the reaction concomitantly increased the chemical yield of silica superstructures (Figure S6a, Supporting Information). This is consistent with a larger number of oil droplets increasing their total surface area and with it the interfacial area between the two immiscible liquids where the superstructures form. Changing the oil phase and surfactant length enabled access to single-layers with varying structures and lattice parameters. Using either mesitylene or hexane instead of cyclohexane also resulted in superstructures with 2D hexagonal pore arrangements, whereas using styrene or chloroform resulted in disordered or stripped patterns (Figure S6, Supporting Information). The lattice parameter of the 2D hexagonal structures decreased linearly with surfactant chain length from C_{18}TAB to C_{12}TAB (Figure S7, Supporting Information). 2D superstructure synthesis could also be realized at a flat liquid-liquid interface in a fully demixed biphasic system under slow stirring (Figure S8, Supporting Information), resulting in large scale superstructures, which fully retained the long-range order. This approach enables scale-up of 2D superstructure synthesis to macroscopic areas, up to the millimeter range in the present work (Figure S9, Supporting Information).

Single-layer silica cage-based superstructures grown at the liquid-liquid interface showed asymmetric chemical properties, corroborating the proposed formation mechanism with amine groups as anchoring points to the liquid-liquid interface (*vide supra*). This was demonstrated by immersing superstructures sitting on carbon coated TEM grids in a solution of citrate-stabilized gold nanoparticles, which are known to readily bind to amine groups[23]. Only some of the superstructures on the TEM grid got functionalized with gold (Figure S10a,b, Supporting Information), however, whereas others remained completely free of nanoparticles. This suggests that amine groups are concentrated on one side of the superstructure, the one in contact with the oil phase during synthesis. Exchanging native citrate ligands with mercaptoundecanoic acid (MUA) allowed the particles to adopt the hexagonal pattern of the silica superstructure, resulting in an ordered array of gold nanoparticles (Figure S10c,d, Supporting Information), which may be of interest for a number of *e.g.* plasmonic or catalytic applications.

Increasing pH above neutral in silica sol-gel reactions accelerates silane hydrolysis rates and decreases condensation rates[24]. At a given time this increases the number of silanol groups, which remain available for longer times. Concomitantly, the increased deprotonation of silanol groups with increasing pH facilitates the interfacial self-assembly by larger coulomb attractive interactions between negatively charged silica clusters and positively charged CTAB surfactants at oil-water interfaces. Together, one would expect these effects to favor the assembly of multilayers, which likely form in a concerted rather than a layer-by-layer fashion. This is exactly what was observed. Silica cage bilayer superstructures could be grown by increasing the amount of ammonium hydroxide by a factor 2 (**Figure 2**). Bilayer domains could be evidenced by lateral views enabled by folds (Figure 2a, b). These bilayers randomly adopted two different structures at roughly equal proportions (Figure 2a). One was the dual structure of an equal sphere close packing (Figure 2c, d). In bulk materials, this corresponds to cubic close packed (ccp) and hexagonal close packed (hcp) structures, whose duals are built from either rhombic dodecahedral (*rd*) or trapezo-rhombic dodecahedral (*trd*) cages for ccp and hcp, respectively[25]. These cages result from their different stacking sequence (ABC and ABAB, respectively), thus with only two layers an ambiguity remains as to what type of cages form these domains. The second bilayer structure was an analog to the clathrate IV structure (Figure 2e,f)[26], which is the dual of the Frank-Kasper Z phase (space group *P*6/*mmm*). It is built from 5^{12}, $5^{12}6^2$ and $5^{12}6^3$ cages assembling into a triangular pattern with the hexagonal faces of the $5^{12}6^2$ cages forming large openings at the corners of each triangle (blue cages in Figure 2f). In contrast to single-layer superstructures, in bilayer domains the cages are now oriented relative to each other, indicating an increase of order in the cage assembly. However, there still remains ambiguity between the two observed structures, which appeared with the same probability.

Further acceleration of silane hydrolysis rates allowed further increases in layer numbers in turn pushing the system into adopting more specific structures throughout the whole material. Further increasing the amount of ammonium hydroxide relative to single-layer conditions by a

factor of 2.5 resulted in superstructures exhibiting a mixture of ccp (space group *Fm*-3*m*) and hcp (space group $P6_3/mmc$) structures (**Figure 3a, b**). From lateral views provided by folds (Figure 3c), these are multilayer structures made of 3 to 4 layers of cages, which is enough to distinguish their stacking sequence along the c axis of the close packing arrangement and impose a specific cage symmetry. The ccp and hcp structures often coexist in 3D bulk mesoporous silica because of their similarity in packing arrangements[14]. Thanks to the limited thickness of the multilayers, ccp and hcp domains could be unambiguously distinguished directly from top views in TEM images (Figure 3a). Lateral views of these superstructures exhibited a square pattern (Figure 3c), consistent with simulated projections for both hcp and ccp structures (Figure 3b).

While these structures result from the close packing of equal spheres, clathrate-like structures result from the topologically close packing of unequal spheres (*vide supra*). We recently demonstrated that increased size dispersion in surfactant micelle systems with added pore expander (*i.e.* oil phase) favors the formation of cage-like mesoporous silica with non-uniform cage structures rationalizing the appearance of the clathrate IV structure at twice the ammonium hydroxide concentration (*vide supra*)[9]. In order to increase the micelle size dispersion and further bias the system towards such structures, we mixed two surfactants of different chain lengths (C_{16}TAB and C_8TAB, see experimental section). In conjunction with a 1.5-fold increase of the amount of ammonium hydroxide relative to single-layer conditions to promote multilayer growth, this indeed resulted in superstructures showing exclusively the clathrate IV structure (Figure 3d-f). The very fine details of the struts forming this structure are consistent with observations from top and lateral views in TEM images (Figure 3d, f, and Figure S11a, Supporting Information). This structure assignment is corroborated by the occasional presence of square defects (Figure S11b, Supporting Information), which are also built from 5^{12} and $5^{12}6^2$ cages with a packing analog to the clathrate I structure (space group *Pm*-3*n*, dual structure of the Frank-Kasper A15 phase), and can arrange well with the triangular pattern of

this structure[8]. Attempts to grow such superstructures thicker by further increasing the ammonium hydroxide concentration (1.8-fold increase) resulted in the appearance of domains analog to the clathrate II structure (space group *Fd*-3*m*, dual structure of the Frank-Kasper C15 phase, Figure S11c, Supporting Information), introducing $5^{12}6^4$ cages sharing their base hexagonal face with the $5^{12}6^2$ cages of the clathrate IV structure. The clathrate IV structure has previously only been observed as a defect layer in bulk *Fd*-3*m* mesoporous silica (clathrate II structure)[14]. In contrast, the growth of a superstructure showing exclusively the clathrate IV structure, instead of the more favorable clathrate II structure, is likely due to the 2D confinement induced by the liquid-liquid interface and limited thickness of the superstructure. This is consistent with the evolution to the clathrate II structure (*Fd*-3*m*) in thicker multilayers, where 2D confinement effects are essentially relaxed resembling the situation in the bulk.

Access to well-defined individual 2D cage-like silica superstructures allows fabrication of heterostacks by tuning the angle between layers, their chemical composition, and structure (**Figure 4a-c**). Figure 4d-h provides examples of bilayer superstructures observed as a result of two single-layer pieces falling on top of each other at different angles, yielding well-defined Moiré patterns in TEM. Such stacks of two superstructures formed, *e.g.* during sample preparation for TEM observations, and a large variety of them, showing angular variations not limited to those illustrated in Figure 4, were found across multiple samples. Figure S10 (Supporting Information) can be regarded as proof-of-principle for assemblies from layers with different chemical compositions. To demonstrate the third degree of freedom, a heterostack with varying structures was formed by mixing two different superstructure samples, one with single-layer superstructure and the other with multilayer clathrate IV superstructure (Figure S12, Supporting Information). In these examples, the heterostacks were formed simply by letting the superstructures fall on top of each other during solvent blotting and evaporation. More active methods can be conceived for the fabrication of these heterostacks such as successive mechanical transfer or Langmuir-Schaefer depositions directly from the liquid-liquid

interface[27]. In this regard, it might be possible to make use of the chemical asymmetry of these superstructures and the versatile functionalization of silica with a large variety of readily available organosilanes, to induce selectivity in stacking mechanisms and to provide cohesion within these heterostacks. We envision that similar to graphene and other 2D electronic materials[28], the ability to control structure and composition in such heterostacks layer by layer will open up a large hitherto unavailable design space for mesoporous silica heterostructures with potential separation or catalytic properties not accessible via conventional homogeneous bulk material synthesis.

Experimental Section

Single-layer silica superstructures: For the single-layer superstructures synthesized under vigorous stirring (Figure 1), cetyltrimethylammonium bromide (CTAB or C_{16}TAB, 50 mg) was first dissolved in water (10 mL) at 60 °C in a round bottom flask. After cooling to room temperature, ammonium hydroxide solution (25 µL, 28-30% in water) and cyclohexane (10 mL) were added under stirring at 1200 r.p.m. After 4 hours, a mixture of TMOS (34 µL) and APTMS (25 µL) was added dropwise, and the reaction was left to proceed overnight at room temperature. For the purification of the superstructures, the reaction mixture was centrifuged (7000 g, 10 min) resulting in the complete demixing of the oil and water phases with the product being located at the interface. The upper and bottom phases were carefully removed with a pipette and the product was dispersed in ethanol (10 mL) with help from an ultrasonic probe sonicator. The superstructures were first washed three times with ethanol (10 mL), followed by sonication and centrifugation (7000 g, 10 min). In order to fully remove the surfactant, the superstructures were then dispersed in a mixture of ethanol (10 mL) and acetic acid (50 µL). After sitting for 20 min, the solution was centrifuged and the superstructures washed another three times with ethanol (10 mL), followed by sonication and centrifugation (7000 g, 10 min). Finally, the superstructures were dispersed in ethanol (5 mL).

For the superstructures synthesized under slow stirring (*i.e.*, with the oil and water phases completely demixed, Figure 2), myristyltrimethylammonium bromide (C_{14}TAB, 10 mg) was first dissolved in water (10 mL) at room temperature in a cylindrical beaker. Then, ammonium hydroxide solution (25 µL) was added to the water phase and cyclohexane (10 mL) was slowly added on top. The stirring was set so that the interface remained essentially flat. Early stage experiments showed that using C_{14}TAB instead of C_{16}TAB helped keeping a smooth interface. In addition, in these experiments the surfactant concentration was kept lower as compared to the syntheses under vigorous stirring in order to account for the smaller surface area between the two phases. Finally, a mixture of TMOS (34 µL) and APTMS (25 µL) was slowly added in the oil phase, directly at the vicinity of the interface with the water phase. After a couple of minutes, flakes of few millimeters in size could be seen at the interface, and were scooped on a glass substrate or TEM grid for fluorescence microscopy or TEM analyses, respectively.

Bilayer and multilayer silica superstructures: The bilayer superstructures (Figure 2) were synthesized using the same procedure as for the single-layer ones, except that 50 µl of ammonium hydroxide solution was added instead of 25 µl. For the multilayer superstructures with mixed hcp (*P*6$_3$*/mmc*) and ccp (*Fm*-3*m*) structures (Figure 3a-c), 62.5 µl of ammonium hydroxide solution was added instead of 25 µl. For the multilayer superstructures with the clathrate structure IV (*P*6*/mmm*) symmetry (Figure 3d-f), 37.5 µl of ammonium hydroxide solution was added instead of 25 µl and a mixture of 17.4 mg of octyltrimethylammonium bromide (C_8TAB) and 25 mg of C_{16}TAB (0.5:0.5 molar ratio, as compared to 1 molar equivalent in the single-layer superstructures synthesis) was used instead of employing C_{16}TAB only as surfactant. The rest of the procedures and purifications were identical as described for the single-layer superstructures synthesis.

Supporting Information
Supporting Information is available from the Wiley Online Library or from the author.

Acknowledgements
This work was funded by the U.S. Department of Energy, Office of Science, Basic Energy Sciences under Award No. DE-SC0010560. K.M. thanks the National Institutes of Health (NIH) for funding under Award No. U54CA199081. T.A. acknowledges financial support from the European Union's Horizon 2020 research and innovation programme under the Marie Sklodowska-Curie grant agreement No 702300. K.W.T. acknowledges financial support from the AcRF Tier 1 grant (2018-T1-001-084) and a startup grant from Nanyang Technological University, Singapore. This work used shared facilities of the Cornell Center for Materials Research, with funding from the NSF Materials Research Science and Engineering Center program (DMR-1719875), as well as the Nanobiotechnology Center's shared research facilities at Cornell.

† Tangi Aubert and Kai Ma contributed equally to this work.

Received: ((will be filled in by the editorial staff))
Revised: ((will be filled in by the editorial staff))
Published online: ((will be filled in by the editorial staff))

References

[1] C. T. Kresge, M. E. Leonowicz, W. J. Roth, J. C. Vartuli, J. S. Beck, *Nature* **1992**, *359*, 710.

[2] M. Templin, A. Franck, A. Du Chesne, H. Leist, Y. Zhang, R. Ulrich, V. Schädler, U. Wiesner, *Science* **1997**, *278*, 1795; D. Zhao, J. Feng, Q. Huo, N. Melosh, G. H. Fredrickson, B. F. Chmelka, G. D. Stucky, *Science* **1998**, *279*, 548.

[3] Y. Sakamoto, M. Kaneda, O. Terasaki, D. Y. Zhao, J. M. Kim, G. Stucky, H. J. Shin, R. Ryoo, *Nature* **2000**, *408*, 449.

[4] Y. Lu, R. Ganguli, C. A. Drewien, M. T. Anderson, C. J. Brinker, W. Gong, Y. Guo, H. Soyez, B. Dunn, M. H. Huang, J. I. Zink, *Nature* **1997**, *389*, 364; A. Walcarius, E. Sibottier, M. Etienne, J. Ghanbaja, *Nat. Mater.* **2007**, *6*, 602; K. E. Shopsowitz, H. Qi, W. Y. Hamad, M. J. MacLachlan, *Nature* **2010**, *468*, 422.

[5] T. Suteewong, H. Sai, R. Hovden, D. Muller, M. S. Bradbury, S. M. Gruner, U. Wiesner, *Science* **2013**, *340*, 337; X. Liu, F. Zhang, X. Jing, M. Pan, P. Liu, W. Li, B. Zhu, J. Li, H. Chen, L. Wang, J. Lin, Y. Liu, D. Zhao, H. Yan, C. Fan, *Nature* **2018**, *559*, 593.

[6] C. E. Ashley, E. C. Carnes, G. K. Phillips, D. Padilla, P. N. Durfee, P. A. Brown, T. N. Hanna, J. Liu, B. Phillips, M. B. Carter, N. J. Carroll, X. Jiang, D. R. Dunphy, C. L. Willman, D. N. Petsev, D. G. Evans, A. N. Parikh, B. Chackerian, W. Wharton, D. S. Peabody, C. J. Brinker, *Nat. Mater.* **2011**, *10*, 389.

[7] N. Kröger, R. Deutzmann, M. Sumper, *Science* **1999**, *286*, 1129.

[8] C. Xiao, N. Fujita, K. Miyasaka, Y. Sakamoto, O. Terasaki, *Nature* **2012**, *487*, 349.

[9] Y. Sun, K. Ma, T. Kao, K. A. Spoth, H. Sai, D. Zhang, L. F. Kourkoutis, V. Elser, U. Wiesner, *Nat. Commun.* **2017**, *8*, 252.

[10] K. Ma, Y. Gong, T. Aubert, M. Z. Turker, T. Kao, P. C. Doerschuk, U. Wiesner, *Nature* **2018**, *558*, 577.

[11] J. Liang, Z. Liang, R. Zou, Y. Zhao, *Adv. Mater.* **2017**, *29*, 1701139.

[12] W. Li, J. Liu, D. Zhao, *Nat. Rev. Mater.* **2016**, *1*, 16023.

[13] E. Phillips, O. Penate-Medina, P. B. Zanzonico, R. D. Carvajal, P. Mohan, Y. Ye, J. Humm, M. Gönen, H. Kalaigian, H. Schöder, H. W. Strauss, S. M. Larson, U. Wiesner, M. S. Bradbury, *Sci. Transl. Med.* **2014**, *6*, 260ra149.

[14] L. Han, Y. Sakamoto, S. Che, O. Terasaki, *Chem.–Eur. J.* **2009**, *15*, 2818.

[15] C. C. M. C. Carcouët, M. W. P. van de Put, B. Mezari, P. C. M. M. Magusin, J. Laven, P. H. H. Bomans, H. Friedrich, A. C. C. Esteves, N. A. J. M. Sommerdijk, R. A. T. M. van Benthem, G. de With, *Nano Lett.* **2014**, *14*, 1433.

[16] K. Ma, C. Mendoza, M. Hanson, U. Werner-Zwanziger, J. Zwanziger, U. Wiesner, *Chem. Mater.* **2015**, *27*, 4119.

[17] K. Ma, H. Sai, U. Wiesner, *J. Am. Chem. Soc.* **2012**, *134*, 13180.

[18] K. Ma, K. A. Spoth, Y. Cong, D. Zhang, T. Aubert, M. Z. Turker, L. F. Kourkoutis, E. Mendes, U. Wiesner, *J. Am. Chem. Soc.* **2018**, *140*, 17343.

[19] Q. Huo, D. I. Margolese, U. Ciesla, D. G. Demuth, P. Feng, T. E. Gier, P. Sieger, A. Firouzi, B. F. Chmelka, *Chem. Mater.* **1994**, *6*, 1176; Q. Huo, R. Leon, P. M. Petroff, G. D. Stucky, *Science* **1995**, *268*, 1324.

[20] K. S. Novoselov, A. Mishchenko, A. Carvalho, A. H. Castro Neto, *Science* **2016**, *353*, aac9439; X. Zhang, J. Grajal, J. L. Vazquez-Roy, U. Radhakrishna, X. Wang, W. Chern, L. Zhou, Y. Lin, P.-C. Shen, X. Ji, X. Ling, A. Zubair, Y. Zhang, H. Wang, M. Dubey, J. Kong, M. Dresselhaus, T. Palacios, *Nature* **2019**, *566*, 368; Y. Cao, V. Fatemi, S. Fang, K. Watanabe, T. Taniguchi, E. Kaxiras, P. Jarillo-Herrero, *Nature* **2018**, *556*, 43.

[21] R. Atluri, Y. Sakamoto, A. E. Garcia-Bennett, *Langmuir* **2009**, *25*, 3189.

[22] P. F. Damasceno, M. Engel, S. C. Glotzer, *Science* **2012**, *337*, 453.

[23] D. V. Leff, L. Brandt, J. R. Heath, *Langmuir* **1996**, *12*, 4723.

[24] C. J. Brinker, *J. Non-Cryst. Solids* **1988**, *100*, 31.

[25] E. A. Lazar, J. Han, D. J. Srolovitz, *P. Natl. Acad. Sci. USA* **2015**, *112*, E5769.

[26] A. J. Karttunen, T. F. Fässler, M. Linnolahti, T. A. Pakkanen, *Inorg. Chem.* **2011**, *50*, 1733.

[27] H. Lim, S. I. Yoon, G. Kim, A. R. Jang, H. S. Shin, *Chem. Mater.* **2014**, *26*, 4891; T. Wen, S. A. Majetich, *ACS Nano* **2011**, *5*, 8868.

[28] K. Kang, K.-H. Lee, Y. Han, H. Gao, S. Xie, D. A. Muller, J. Park, *Nature* **2017**, *550*, 229.

FIGURES

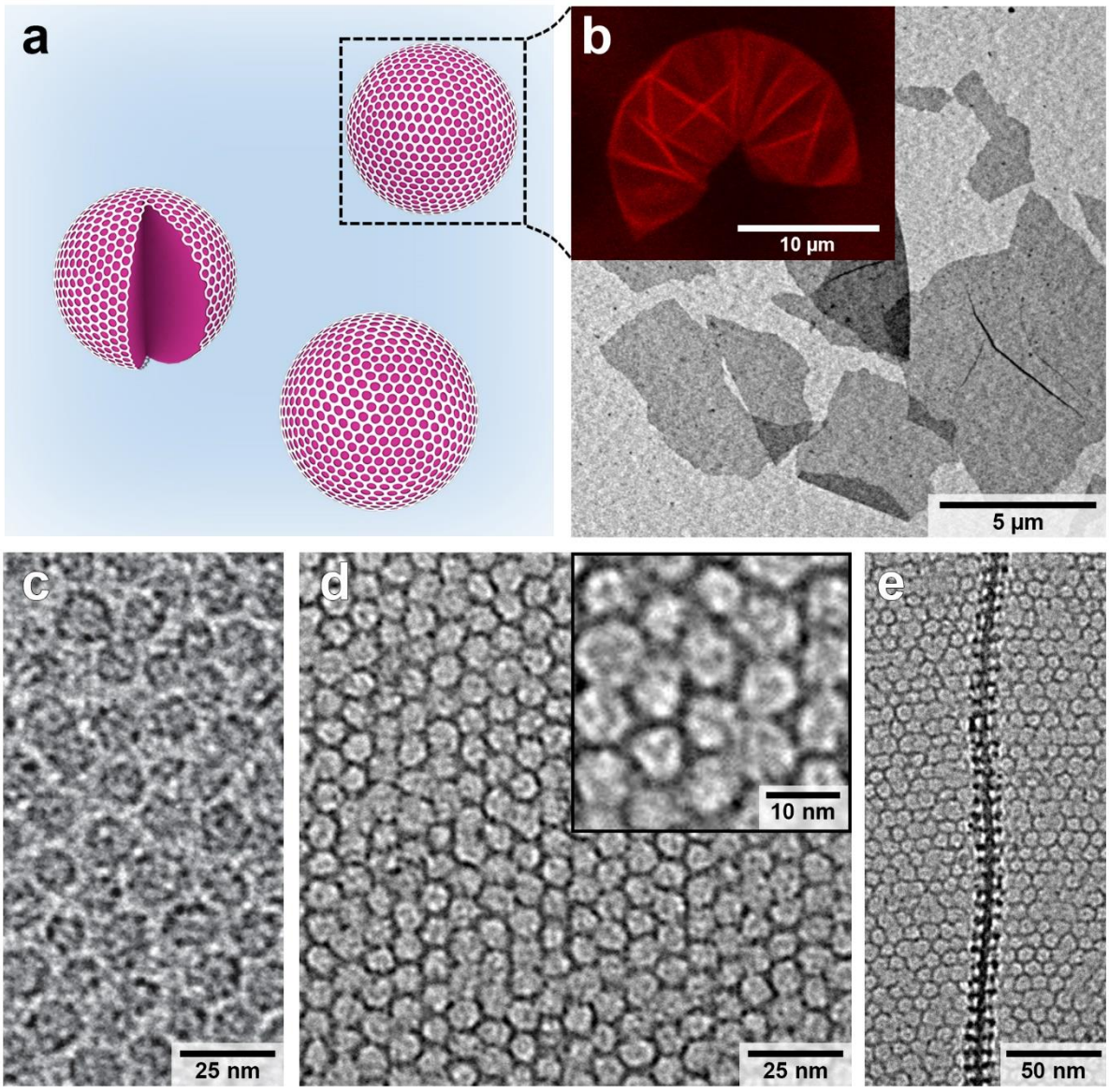

Figure 1. a, Illustration of silica superstructure formation at the surface of large oil droplets. **b,** Low magnification TEM image of as prepared silica layer showing folds only in larger (> 5 µm) pieces (inset: fluorescence microscopy image of a partially preserved fluorescently stained silica layer grown around a vesicle). **c-d,** High magnification TEM images of isolated silica cages (**c**) and a silica cage superstructure with well-ordered honeycomb structure (**d,** inset: zoom-in on the cage structures within the superstructure). **e,** TEM image of a single-layer fold providing a double lateral view of the superstructure.

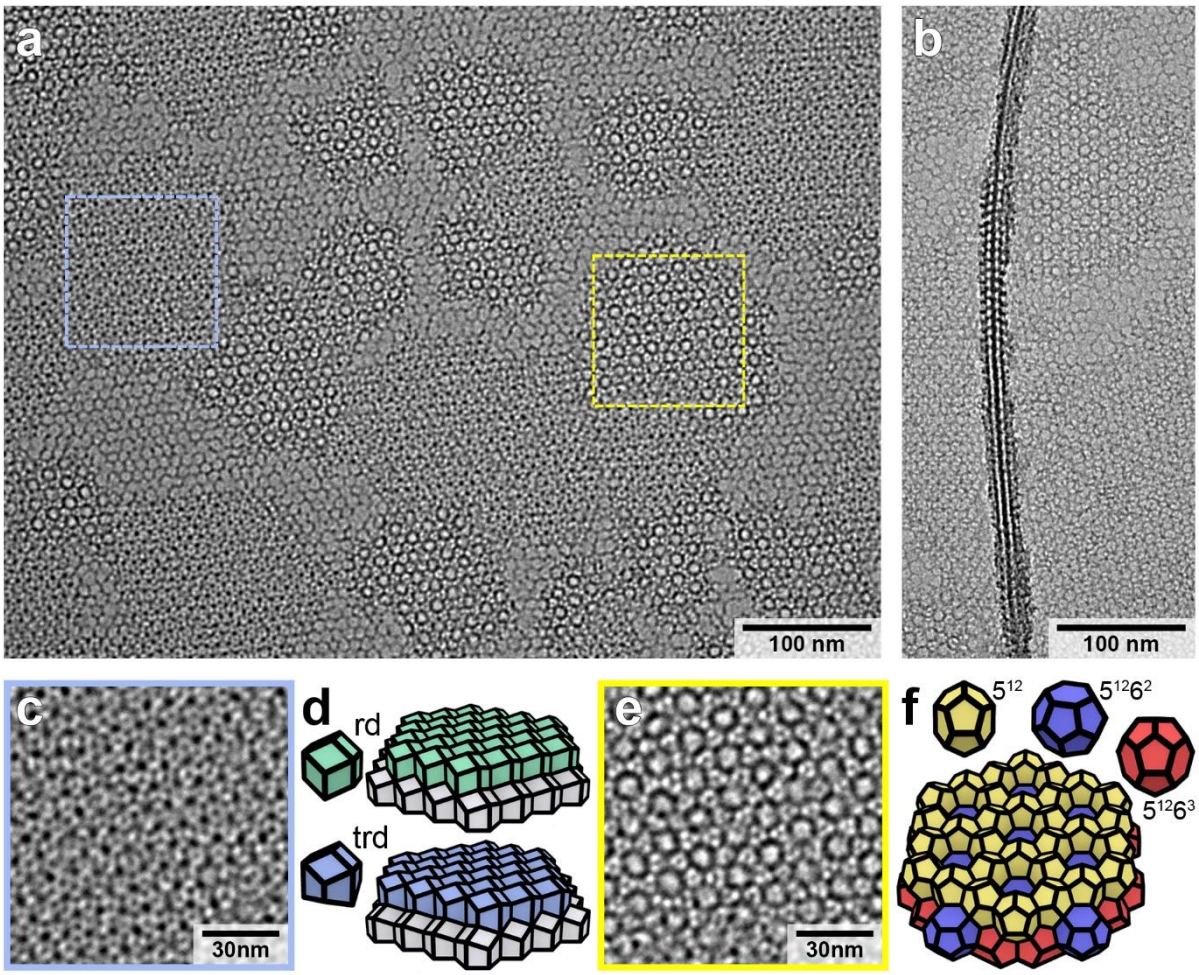

Figure 2. a-b, TEM images of a superstructure with bilayer islands (**a**) and corresponding lateral view from a fold (**b**). **c-f,** TEM zoom-ins (**c and e**) and illustrations (**d and f**) of bilayers resulting from the close packing of equal spheres, built from either rhombic dodecahedral (*rd*) and trapezo-rhombic dodecahedral (*trd*) cages (**c,d**), or from the packing of unequal spheres, built from 5^{12}, $5^{12}6^2$, and $5^{12}6^3$ cages (**e and f**).

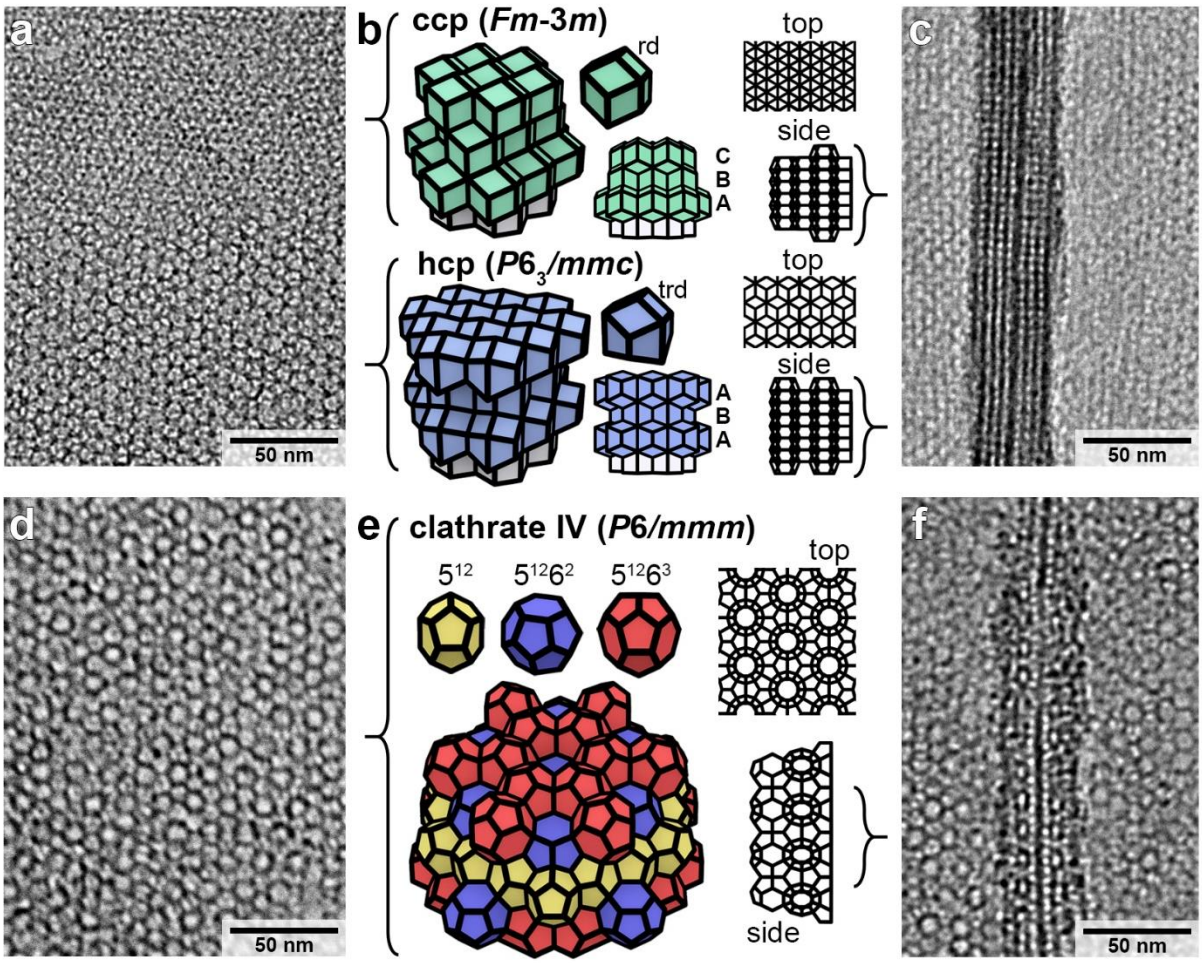

Figure 3. a, TEM image of a superstructures exhibiting ccp (upper part) and hcp (lower part) structures. **b,** Illustration of ccp (top) and hcp (bottom) structures built from rhombic dodecahedral (*rd*) and trapezo-rhombic dodecahedral (*trd*) cages, respectively, and representative simulated top and side view projections. **c,** TEM image of a fold in a hcp/ccp superstructure providing a double lateral view. **d,** TEM image of a superstructure exhibiting the clathrate IV structure. **e,** Illustration of the corresponding superstructure derived from three different cage motifs and simulated top and side view projections. **f,** TEM image of a fold in a clathrate IV superstructure providing a double lateral view.

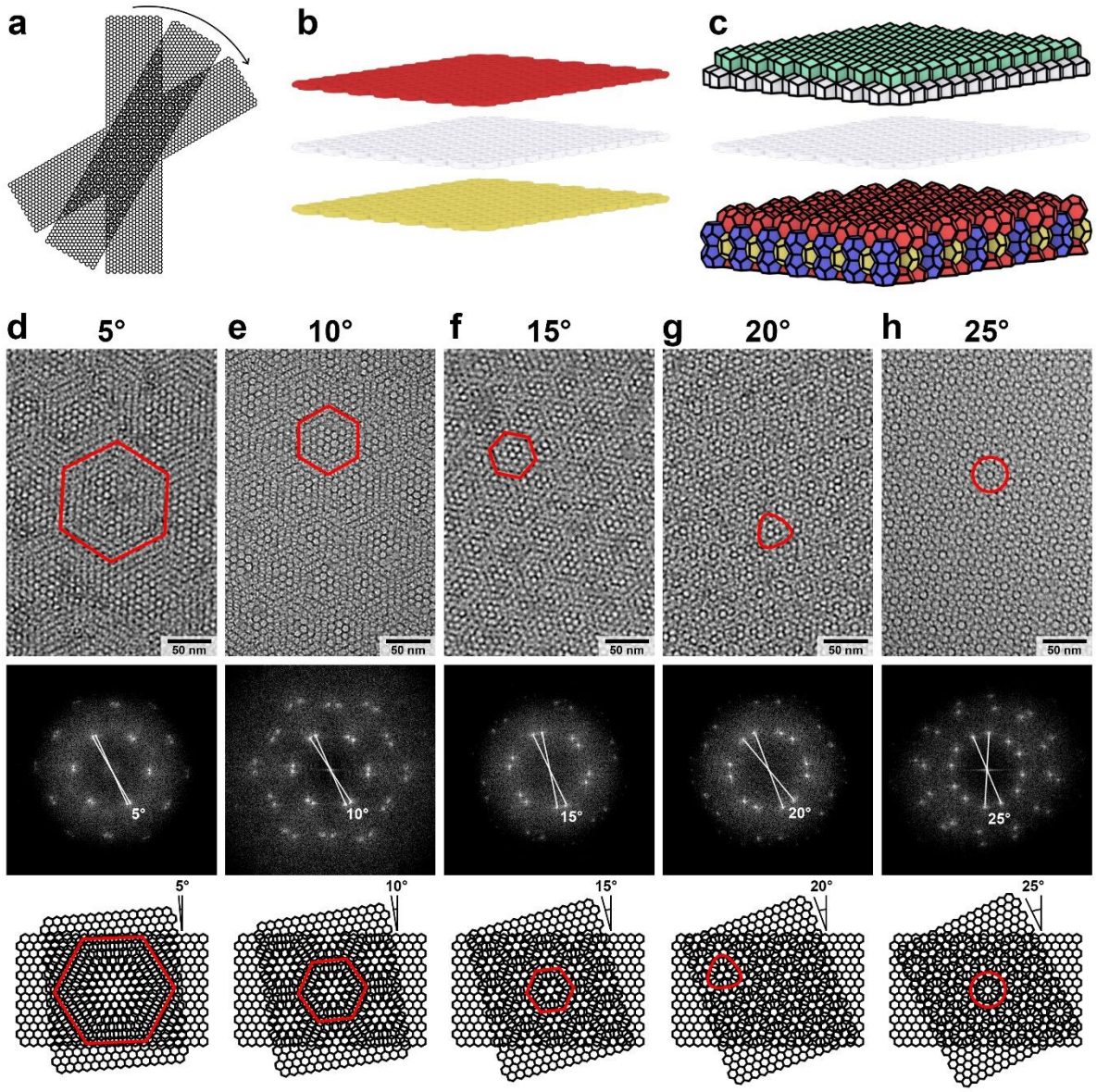

Figure 4. a-c, Illustration of superstructure heterostack designs by tuning the angle between layers (**a**), their chemical composition (**b**), and structure (**c**). **d-h,** Moiré patterns resulting from two single-layer cage superstructures stacking at different angles. TEM images (top), corresponding FFTs (middle), and simulated projections (bottom) of two superstructures at angles of 5° (**d**), 10° (**e**), 15° (**f**), 20° (**g**), and 25° (**h**). In both the TEM images and simulated projections easily identifiable motifs of the Moiré patterns are highlighted in red.